Research Article Vol. 61, No. 30 / 20 October 2022 / Applied Optics 8959

applied optics

Utilizing broadband wavelength-division multiplexing capabilities of hollow-core fiber for quantum communications

Umberto Nasti,[1,*] Hesham Sakr,[2,3] Ian A. Davidson,[2] Francesco Poletti,[2] and Ross J. Donaldson[1]

[1]Institute of Photonics & Quantum Sciences, Heriot-Watt University, Edinburgh EH14 4AS, UK
[2]Optoelectronics Research Centre, University of Southampton, Highfield Campus, SO17 1BJ Southampton, UK
[3]Lumenisity Ltd., Unit 7, The Quadrangle, Southampton, SO51 9DL, UK
*Corresponding author: U.Nasti@hw.ac.uk

Received 1 August 2022; revised 6 September 2022; accepted 12 September 2022; posted 13 September 2022; published 14 October 2022

One of the major challenges in the deployment of quantum communications (QC) over solid-core silica optical fiber is the performance degradation due to the optical noise generated with co-propagating classical optical signals. To reduce the impact of the optical noise, research teams are turning to new and novel architectures of solid-core and hollow-core optical fiber. We studied the impact when co-propagating a single-photon level (850 nm) and two classical optical signals (940 nm and 1550 nm) while utilizing a nested antiresonant nodeless fiber (NANF) with two low-loss windows. The 940 nm signal was shown to impact the single-photon measurement due to the silicon detector technology implemented; however, multiplexing techniques and filtering could reduce the impact. The 1550 nm signal was shown to have no detrimental impact. The results highlight that both high bandwidth optical traffic at 1550 nm and a QC channel at 850 nm could co-propagate without degradation to the QC channel.

https://doi.org/10.1364/AO.471632

1. INTRODUCTION

Quantum key distribution (QKD) [1–5] is a mature application of quantum information science that enables the secure distribution of encryption keys and is one among many quantum communications protocols [6–8].

Over the past couple of decades, QKD has seen continuous developments that have improved performance through new protocol variations [9] and the application of new enabling technologies [10,11]. QKD is now making a transition from lab-based experiments into the real world where network integration [12–16] and long-distance capabilities are being investigated [15,17]. Despite significant research progress, QKD still has challenges in real-world implementation.

One obstacle is the cost of optical fiber network deployment. If QKD channels can be integrated into the existing communication network architectures, the total cost of a QKD link may be greatly reduced. This means that QKD channels should be able to co-propagate with classical data channels in the same fiber using multiplexing techniques, such as wavelength-division multiplexing (WDM) [18–22], without suffering significant penalties from optical cross talk [18], suffering noise from Raman scattering [19], and/or compromising the security.

While expensive, government initiatives to boost internet connectivity and bandwidth mean that the deployment of new optical fiber or replacing existing optical fiber will continue.

By exploiting new optical fiber technologies, [20,21], in future deployment, there is a real prospect to improve the coexistence of classical and QKD channels utilizing spatial [22,23], mode [24], and WDM techniques.

In recent years, new types of optical fiber that confine light in a hollow air or vacuum filled core surrounded by a microstructure cladding have attracted considerable attenuation. These new fibers are typically termed as hollow-core fibers (HCFs). Nested antiresonant nodeless fibers (NANFs) [25,26], a specific type of HCF, have shown the potential to transmit low-latency optical signals over narrow and broad spectral ranges with a low loss [27] making them an interesting candidate for QKD protocols [28].

Of particular interest for QKD is the ability to customize NANFs to transmit with multiple low-loss spectral windows, where a window occurs in the visible/near-infrared (NIR) [29] and another occurs in the telecommunication band 1550 nm [27,30], enabling quantum and classical signals to be spectrally separated, negating concerns for additional noise from the classical signals.

Here, we present the demonstration of a NANF as the transmission channel for three different wavelengths: single-photon level, pseudo-quantum signal at a wavelength of 850 nm, and two co-propagating classical signals at wavelengths 940 nm and 1550 nm.

Using a 5 m length of NANF, we show the impact of the two classical wavelengths on a silicon single-photon avalanche diode (Si-SPAD) used for measuring the single-photon level signal.

While the 1550 nm signal does not increase the noise on the Si-SPAD, we do see an increase in noise due to the 940 nm signal as the Si-SPAD is responsive to that wavelength. The noise from the 940 nm is attributed to the spectral splitting of dichroic spectral filters and would be present with a solid-core optical fiber. Overall, we demonstrate the feasibility of transmitting high data rates at 1550 nm while transmitting QKD signals in the NIR.

By utilizing this new type of NANF and relatively inexpensive Si-SPAD technology, there could be a reduction in the cost of deploying short range QKD networking, enabling more uptake of the technology if these particular NANFs are utilized in local optical fiber networks.

2. NESTED ANTIRESONANT NODELESS FIBER

The NANF used in this work has been fabricated and characterized by the University of Southampton. Figure 1 shows an optical microscope image of the cross section of the NANF core used in this work. The fiber consists of a hollow core of 29.3 μm diameter and contain five outer and nested silica tubes of 26.6 μm and 11.6 μm diameter, respectively. The thickness of the silica tubes was 0.6 μm.

In this configuration, the light is confined in the core by the surrounding membranes via antiresonance. Adding nested tubes, with the same membrane thickness, has the effect of reducing the confinement loss of the fiber and makes them less sensitive to bend-induced loss when deployed.

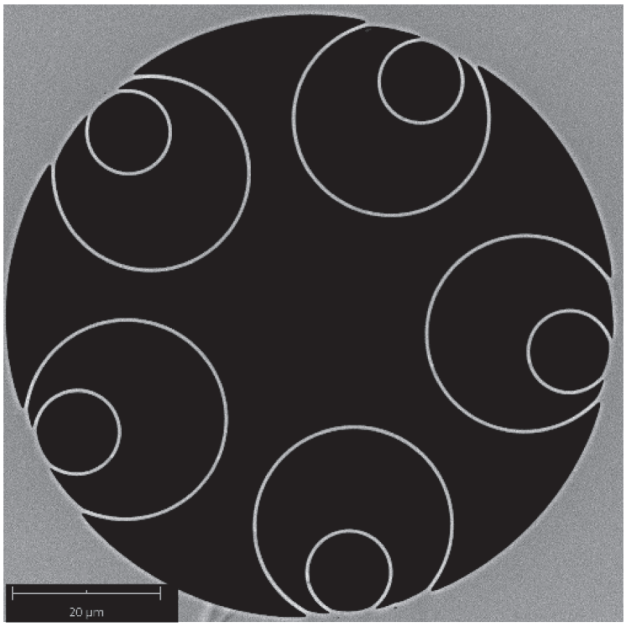

Fig. 1. Cross section of the nested antiresonant nodeless fiber (NANF) fabricated by the University of Southampton. The image was taken by an optical microscope. The fiber was composed of five glass tubes with five internal glass tubes of 0.6 μm thickness. The core of the fiber was 29 μm.

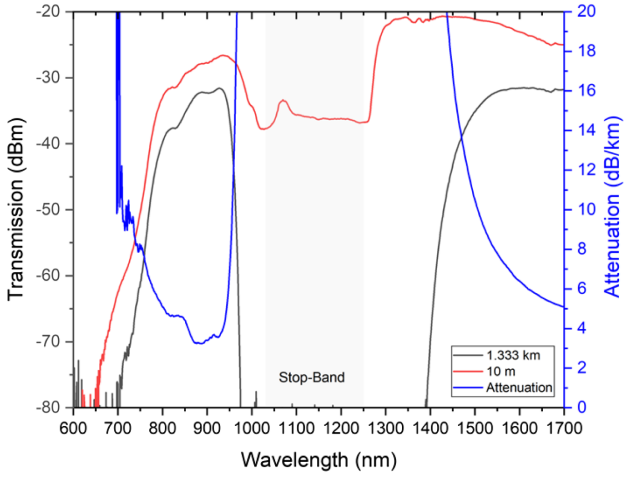

Fig. 2. Cutback loss and transmission plots for 10 m and 1.333 km nested antiresonant nodeless fiber (NANF) in the 600–1800 nm wavelength range. Losses for 850 nm, 940 nm, and 1550 nm are, respectively, 4.5 dB/km, 4.3 dB/km, and 7.9 dB/km.

The structure of this fiber provides low-loss transmission at 850, 940, and 1550 nm wavelengths in its fundamental (LP01) mode. Figure 2 shows the loss and transmission against wavelengths from 600–1700 nm.

The loss was measured via the standard cutback method, where the full fiber band (1.333 km) was cut back to 10 m while the launch was kept constant.

The optical losses for 850 nm, 940 nm, and 1550 nm were 4.5 dB/km, 4 dB/km, and 7.9 dB/km, respectively. The wavelength independent mode field diameter (MFD) of the fiber was 19.6 μm. The experiment utilized a 5 m length of fiber to demonstrate the concept of transmitting multiple wavelengths.

3. OPTICAL SETUP

The scheme of the experimental setup realized the coupling of the three wavelengths (850, 940, and 1550 nm) into the NANF as shown in Fig. 3. All three sources used in this work were gain-switched laser diodes enabling both continuous-wave (CW) and pulsed operation.

A central time-correlated single-photon counting (TCSPC) module was used to generate the trigger signals for the lasers and measure the single-photon time of arrival from the Si-SPAD detector.

The 1550 nm laser diode was not pulsed in the experiments to allow us to simulate bandwidth traffic that was at a much higher repetition rate than the single-photon signal. The optical signal was fiber coupled into a polarization maintaining (PM) optical fiber prior to the free-space wavelength combination.

The 940 nm laser diode was utilized in two operations, CW and pulsed. In pulsed mode, the laser was triggered by the TCSPC module with a square pulse at an operational frequency of 1 MHz and a pulse width of 20 ns.

When the source was gain-switched, the optical properties followed the same shape. The 940 nm optical signal was fiber

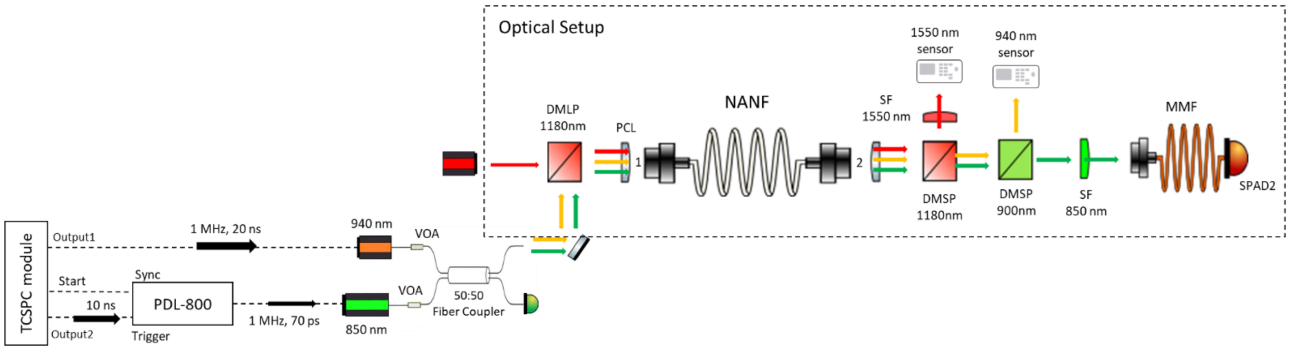

Fig. 3. Scheme of the experimental setup used to measure the coupling efficiency of the nested antiresonant nodeless fiber (NANF) with the quantum (850 nm) and two classical (940 and 1550 nm) signals and to test the operation of the fiber in the single-photon regime. The pulsed 850 nm and the 940 nm lasers were triggered by the time-correlated single-photon counting (TCSPC) module at an operational frequency of 1 MHz and a signal width of 10 ns for the 850 nm source and 20 ns for the 940 nm source. Both optical signals were attenuated using independent variable optical attenuators (VOA) and then were coupled together by a 50:50 fiber coupler. One output of the 50:50 coupler was connected to a single-photon avalanche diode (SPAD 1) to monitor the mean photon number per pulse. The other output of the 50:50 coupler was coupled to a fiber-collimator. The coaligned 850 and 940 nm optical signals were combined with the continuous-wave 1550 nm source with a free-space long-pass dichroic (DMLP 1180 nm). After wavelength combination, the light was then focused into the NANF using an uncoated plano–convex lens (PCL) 60 mm focal length. Light then propagated through the 5 m length of NANF. The same lens was positioned at the exit of the NANF to collimate the output light, which then propagated to a series of short-pass dichroic splitters that reflected 1550 nm (DMLP 1180 nm) and 940 nm (DMSP 900 nm) to their respective photodiode power sensors. The 850 nm signal was coupled to another SPAD (SPAD 2) via a 400 μm core multimode fiber (MMF). Spectral filters (SFs) were used after each DMSP to further isolate 850 nm and 1550 nm from 940 nm. Numbers 1 and 2 are the positions of the photodiode power sensors used to measure the power of each optical signal (1) before and (2) after the NANF.

coupled and attenuated using a manual variable attenuator to set various optical power levels.

The single-photon, pseudo-quantum, level optical signal was generated by a gain-switched laser diode, which emitted polarized photons at a wavelength of 850 nm.

The central TCSPC module triggered the laser's driver board with a 10 ns wide pulse at an operational frequency of 1 MHz, which then created an optical pulse that was <70 ps wide.

The optical signal was coupled into a single-mode fiber where the polarization was aligned to PM fiber, providing a polarization reference. The optical signal was then attenuated to the single-photon per pulse level using an electrical variable attenuator.

To ease the optical alignment, the 850 nm and 940 nm were combined using a 50:50 PM fiber coupler. One of the outputs was connected to a SPAD 1 to monitor the mean photon number (MPN) per pulse prior the NANF. A long-pass dichroic mirror (cutoff wavelength at 1180 nm) was used to combine the 850/940 nm and 1550 nm in free space prior to the NANF.

To couple the three wavelengths into the NANF, an uncoated plano–convex lens (PCL), with focal length 60 mm, mounted on an $x/y/z$ stage was used. The same configuration is installed at the end of the fiber to collimate three optical signals out of the NANF.

The output collimated optical signals were spectrally separated via a combination of two short-pass dichroic mirrors (DMSP). DMSP 1180 nm reflects 1550 nm to a power sensor, while DMSP 900 nm reflects 940 nm to another power sensor.

A 1550 nm spectral filter (12 nm FWHM) was attached to DMSP 1180 nm to isolate the 1550 nm beam. In the same way, an 850 nm spectral filter (10 nm FWHM) was attached to DMSP 900 nm to isolate 850 nm from 940 nm.

Table 1. Single-Photon Detection Efficiency at 850 nm and 940 nm, Dark Count Rate, and Dead Time of Single-Photon Avalanche Diode Counting Modules as Reported in Their Datasheet

	SPDE at 850 nm	SPDE at 940 nm	DCR (cps)	Dead Time (ns)	Active Area Diameter (μm)
SPAD 1	40%	22%	500	28	180
SPAD 2	40%	22%	180	45	100

The transmitted pulsed 850 nm beam was coupled to another SPAD (SPAD 2) via a 400 μm core multimode fiber (MMF).

The large core was used to ease optical alignment; however, this did lead to optical losses due to overfilling the Si-SPAD detector active area. Table 1 lists characteristics of SPAD modules according to their datasheet.

4. EXPERIMENTAL DETAILS

This section discusses a specific experimental procedure and presents experimental results for the optical loss of the NANF, the single-photon characterization of the 850 nm signal, and the noise contribution to the single-photon detector from the two co-propagating wavelengths.

A. Optical Loss

To measure the power loss of the optical setup, the power of each laser beam was measured by a photodiode power sensor in two points: (1) before the NANF positioning the sensor outside the DMLP 1180 nm and (2) after the NANF positioning the sensor outside the fiber. These points are highlighted in Fig. 3.

Table 2. Comparison of the Experimental Optical Power Loss of the Nested Antiresonant Nodeless Fiber and at the End of the Optical Setup with the Theoretical Power Loss Inside 5 m NANF[a]

λ (nm)	Theoretical Loss (dB/km)	Loss Inside 5 m Fiber (dB)	Power before NANF (μW)	Power Out NANF (μW)	Loss (dB)
850	4.5	0.0225	2	0.7	4.5
940	4.3	0.02	153	61	4
1550	7.9	0.0395	913	275	5.2

[a]High loss in this experiment was due to coupling into the NANF.

To measure the power of 1550 nm and 940/850 nm optical paths, two different power sensors were used. Table 2 compares the experimental power loss from the input to the output and theoretical loss of the 5 m NANF calculated using values shown in Fig. 2. The optical loss for each wavelength was 4.5 dB at 850 nm, 4 dB at 940 nm, and 5.2 dB at 1550 nm.

It is well known that, for a good fiber coupling, the MFD should be matched to the diffraction-limited spot size given by the following equation:

$$\mathrm{MFD} = \frac{4f\lambda}{\pi D}, \tag{1}$$

where f is the focal length of the lens (in our experiment 60 mm), D is the diameter of the collimated beam, and λ is the wavelength of light. Using value of the collimator datasheet, the MFD for 850/940 nm was 37.3 μm while for 1550 nm is 74 μm. Since these values do not match the MFD of the NANF (19.6 μm), while the MFD accounted for part of the loss, the other contribution came from the angular misalignment due to the resolution of the free-space stages.

B. Single-Photon Regime

To test the operation of the NANF in the single-photon regime, a pulsed 850 nm laser was attenuated, and a MPN below 0.5 photons per pulse was set. That number is in accordance with the value used for many weak-coherent pulse QKD demonstrations [31,32].

The MPN was set while the 940 nm and 1550 nm laser were inactive. Figure 4 shows the relation of the single-photon count rate measured for each SPAD detector against the voltage applied to the electric variable optical attenuator. The difference between count rates is due to the optical channel loss difference between the two detectors, which is 14.3 dB. That loss was an accumulation from the NANF, coupling to the 400 μm core MMF and the coupling of the MMF to SPAD 2, which had a smaller active area to the MMF illumination.

The number of incident photons per pulse is calculated by the following equation:

$$\text{Photon per pulse} = \frac{(\mathrm{CR}\cdot f) - \mathrm{DCR}}{(\mathrm{DE}/100)} * \nu, \tag{2}$$

where ν is the frequency of the input laser and CR is the raw count rate measured by the detector. The raw count rate was monitored by the TCSPC module. DCR and DE are, respectively, the dark count rate and the detection efficiency of the SPADs.

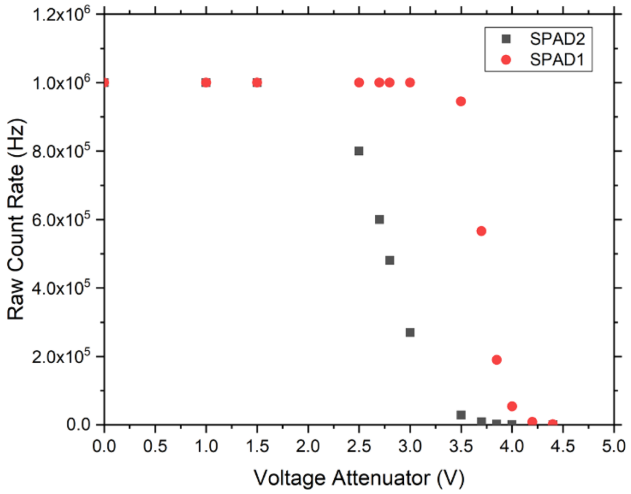

Fig. 4. Incident 850 nm photon count rate measured at the beginning of the optical setup (SPAD1, red) and at the end of the optical setup (SPAD2, black) against the voltage applied to the electrical variable optical attenuator. The nonlinear plot achieved is in accordance with the transmission graph of the attenuator datasheet.

Table 3. Number of Photons per Pulse Measured at (1) the Beginning of the Optical System and (2) the End of the Optical System for Different Attenuations of the 850 nm Pulsed Laser[a,b]

Attenuation (V)	Count Rate SPAD1 (MHz)	Photon Per Pulse 1	Count Rate SPAD2 (MHz)	Photon Per Pulse 2
0	1	2.6	1	2.62
2.5	1	2.6	0.8	2.1
2.7	1	2.6	0.6	1.54
2.8	1	2.6	0.481	1.23
3	1	2.6	0.27	0.7
3.5	0.945	2.4	0.029	0.07
3.7	0.566	1.4	0.0009	0.02
3.85	0.19	0.5	0.00023	0.0055
4	0.54	0.1	660×10^{-6}	0.0014
4.2	0.0085	0.02	180×10^{-6}	0.0002
4.4	0.0017	0.003	100×10^{-6}	$1.1 \cdot 10^{-9}$

[a]$\nu = 1$ MHz.
[b]The number of photons per pulse was calculated by Eq. (2).

The correction factor f is given by the following:

$$f = \frac{1}{1 - (t_D * \mathrm{CR})}, \tag{3}$$

where t_D is the dead time of the SPAD. The single-photon regime is achieved when the attenuator is biased 4 V corresponding to 0.1 photons per pulse input (see Table 3).

Loss of the optical system reduces the number of 1.4×10^{-3} photons per pulse. In this condition, the count rate detected at the end of the optical system is more than 600 Hz. Another parameter to confirm the single-photon regime is the calculation of the timing jitter of the SPAD2.

Since the distribution of counts between the laser input and signals detected typically shows a Gaussian profile, the timing

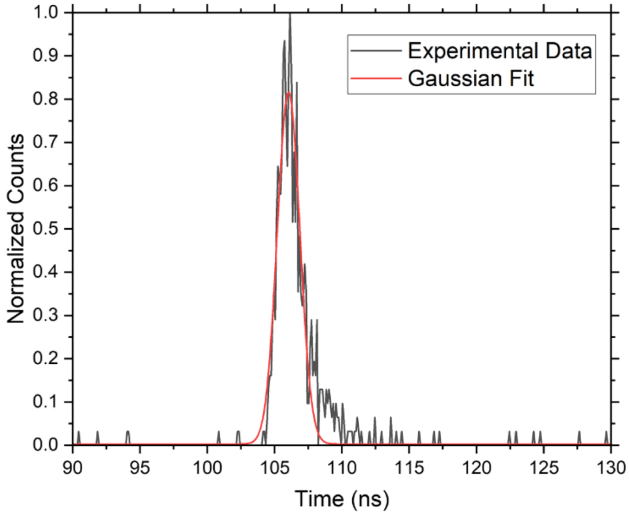

Fig. 5. Experimental normalized distribution of counts versus time between the 850 nm laser signal input ("Start") and that detected by SPAD2 ("Stop"). The laser power is attenuated into the single-photon regime biasing the attenuator to 4 V. Timing jitter is given by the full width at half-maximum (FWHM) of the Gaussian curve fitting corresponding to 1.97 ± 0.02 ns.

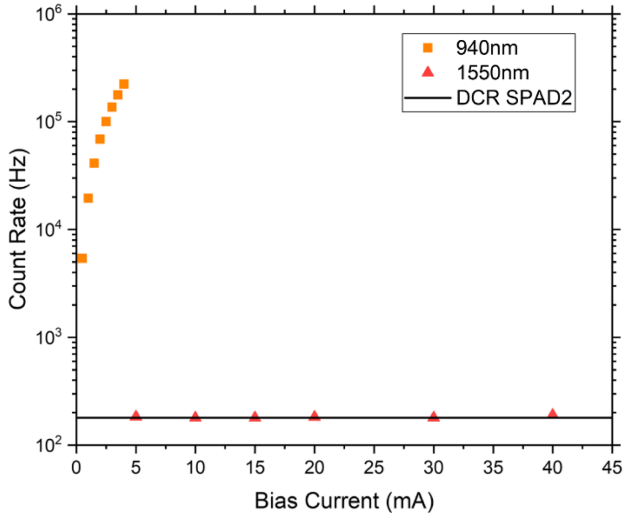

Fig. 6. Count rate of 940 nm (orange) and 1550 nm (red) laser diodes detected by SPAD2. The black line represents the noise of the detector. Enhancing the bias current of laser diodes, we note that the 940 nm laser exhibits high values of the count rate while 1550 nm does not affect the system exhibiting a count rate of 180 cps, which is comparable with the dark count of SPAD2 (black line).

jitter is obtained from the FWHM of the Gaussian fitting curve as shown in Fig. 5. The value calculated was 2 ns in accordance with the datasheet of the SPAD.

C. Noise with Continuous-Wave Operation

The impact of co-propagating both laser sources with the characterized single-photon level signal was performed in two steps: with both laser in CW mode and with the 940 nm in pulsed mode while the 1550 nm remained in CW. The CW 1550 nm allowed the simulation of a high bandwidth optical channel.

Figure 6 shows the measured raw count rate on SPAD 2 while the bias voltage driving the CW operation of the 940 and 1550 nm was increased. The measurements were taken while the single-photon level source was inactive to highlight the contributions from the CW sources.

It can be seen that, while the 940 nm laser does add significant noise, the 1550 nm signal does not increase the noise on the detector.

The independence of 1550 nm and power dependence of 940 nm are not unexpected as the SPADs are silicon, meaning they are responsive up to around 1 μm. The results highlight that high bandwidth co-propagating traffic at 1550 nm could coexist with a single-photon channel in the NIR; however, wavelengths that are closer to the quantum signal will need other isolation mechanisms to co-propagate.

In terms of spectral isolation, the dichroic splitter DMSP 900 nm had a 0.163% transmission at 940 nm power. That light is transmitted to SPAD 2, which had a spectral efficiency of approximately 20% at 940 nm (see Table 1). Further spectral filtering could be incorporated with other spectral filters to reduce the impact of the 940 nm signal. The noise is due to the technical implementation and would also be seen when utilizing a solid-core fiber.

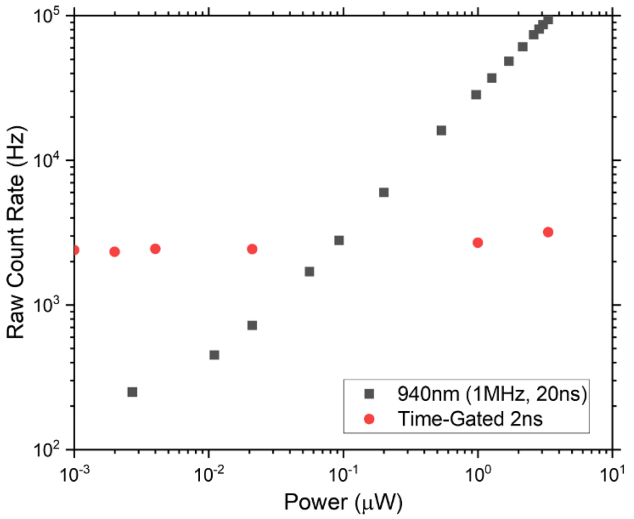

Fig. 7. Raw count rate of the 940 nm laser diode modulated as the pulse of 1 MHz frequency and 20 ns pulse width (black) and of the 850 nm quantum signal around 2 ns time-gating (red). Attenuating the laser beam, the count rate is highly decreased to 200 Hz.

D. Noise with Pulse Source

In this experiment, we show the impact of a pulsed and temporally separated 940 nm signal on the single-photon level signal. The 940 nm laser was pulsed at the same operational frequency as the 850 nm laser (1 MHz). As the 1550 nm source did not impact at any optical power available, it is negated for the discussions in this section.

Figure 7 shows the raw count rate when pulsed and the raw count rate when time-gating with a 2 ns window around the quantum signal. There is a significant reduction in noise when utilizing the pulsed a temporal spaced classical signal.

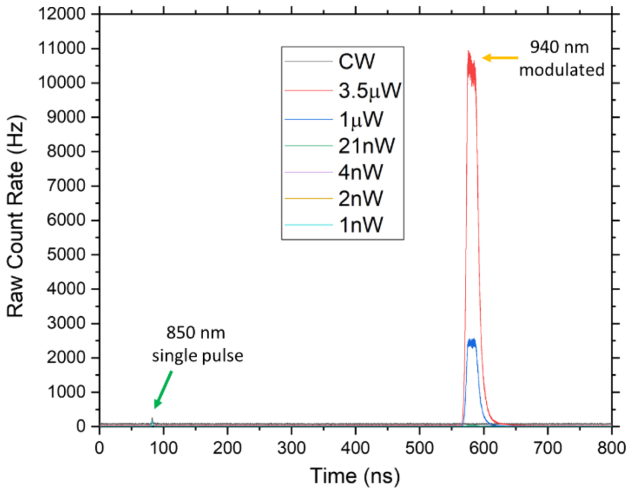

Fig. 8. Distribution of time delay between the 850 nm laser signal input ("Start") and that detected by SPAD2 ("Stop") when 940 nm is turned on. When the 940 nm laser beam is modulated as a pulsed laser of 1 MHz frequency and 20 ns pulse width, the graph exhibits the pulse of the modulated 940 nm that is time-separated from the 850 nm single-photon level signal.

By improving pseudo-quantum signal isolation through narrower time-gating and narrower spectral filtering, the noise could be reduced further.

In QKD experiments, teams typically incorporate time-gating to reduce the background noise. As the 940 nm was pulsed, the majority of the photons arrived at SPAD 2 at a fixed time period.

Utilizing temporal separation, the raw count rate in the QKD time-gated region can be reduced. Utilizing the TCSPS module, a histogram was created to identify the pulse position of the 850 nm and 940 nm signals. A time-delay separation of about 510 ns was then applied to the electrical trigger of the 940 nm laser, time-seperating the single-photon level and classical laser pulses.

Figure 8 shows the histogram of the quantum signal 850 nm and the 940 nm in both the CW and modulated signal.

The plot shows that the noise from the 940 nm signal is primarily temporally separated from the single-photon signal.

Figure 9 shows a zoomed-in plot to each pulse: the quantum pulse 850 nm in Fig. 9(a) and the modulated 940 nm in Fig. 9(b).

When the 940 nm is in CW mode (3 nW input power), this generates a blanket background noise across adding noise to the time-gate window for a QKD signal.

Even with time-gating, the noise is broadband, meaning a large proportion is within a time-gate window. When pulsed, temporal separation and time-gating can reduce noise on the detector.

Although the count rate on the detector remains high, the majority of the photons are concentrated in the optical pulse, and time-gating helps to reduce the contribution of noise to the single-photon level signal.

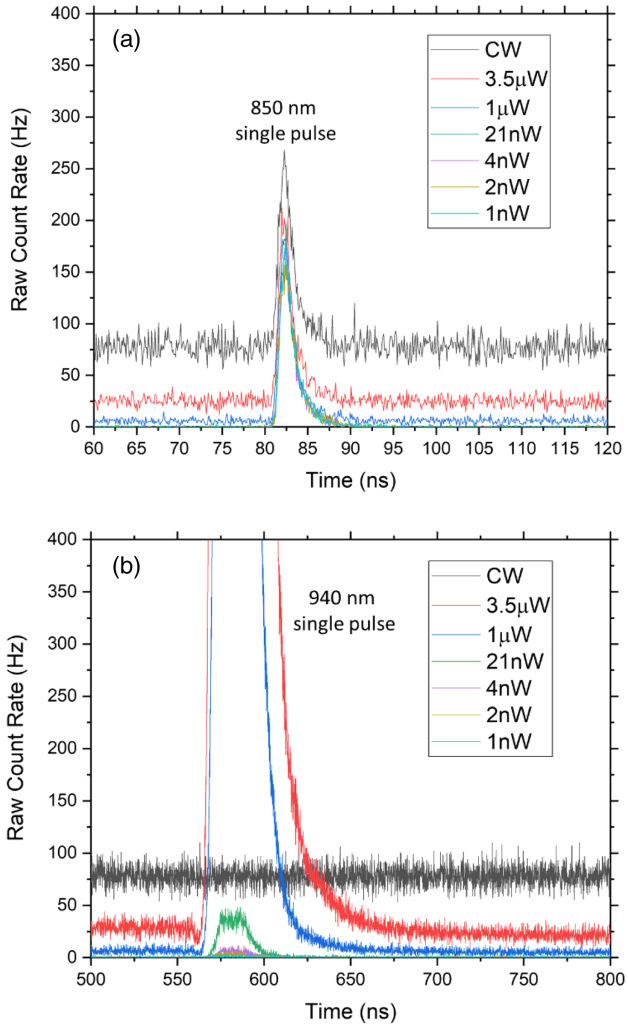

Fig. 9. Enlargement of Fig. 8. These plots show, respectively, (a) the quantum signal 850 nm and (b) the 940 nm signal in CW and modulated mode. The CW component (black) generates high background noise to the quantum signal. When the 940 nm laser is modulated (red), the background noise is reduced. Attenuating the power of the modulated 940 nm laser diode below 3 nW (CW condition), the pulse is reduced in respect to 850 nm single pulse reducing noise.

5. CONCLUSION

In optical fiber-based QKD, co-propagation of classical optical signals can lead to an increase in optical noise for the quantum channel, which is detrimental to the performance, especially in the high loss regime. WDM techniques have shown a benefit to co-propagate classical signals; however, when utilizing traditional solid-core silica-fiber, increasing optical power, equivalent to increasing bandwidth, eventually leads to high Raman noise that swamps the QKD signal.

SDM techniques, which spatially separate the quantum signal, have also been investigated, and it opens the question to the development of new fibers to enable QKD to be deployed efficienly.

In this paper, we have utilized a 5 m length of NANF, which has two broadband low-loss windows, to demonstrate the

impacts of co-propagating three optical wavelengths: a single-photon level, pseudo-quantum signal at 850 nm; a CW and pulsed 940 nm classical signal; and a CW 1550 nm signal.

We show that the 1550 nm source does not impact the noise on the Si-SPAD, meaning high bandwidth traffic at that wavelength could co-propogate with a QKD signal without being detrimental to a QKD protocol. The 940 nm signal does increase the noise on the Si-SPAD as the Si-SPAD is still responsive to that wavelength.

However, we highlight that temporal filtering could be used to reduce the impact of the 940 nm signal. Further isolation of the single-photon level signal, with narrower time and spectral filters, would further reduce the impact. The impact of the 940 nm laser would also be seen with a solid-core fiber, as the noise is due to spectral separation rather than the optical fiber transmission.

Our results highlight that NANFs could be a viable solution to aid in the uptake of co-propogating classical and quantum channels in optical fiber networking as the broadband low-loss optical windows enable co-propagation of quantum and classical signals that could be spectrally separated, resulting in no single-photon detector sensitivity for the classical optical signals. There is an advantage in cost when using Si-SPAD; therefore, a fiber with a low-loss window in the visible or NIR should enable cheaper solutions for QKD networking.

Funding. Engineering and Physical Sciences Research Council (EP/P030181/1, EP/T001011/1); Royal Academy of Engineering (RF\201718\1746); European Research Council (682724).

Acknowledgment. The Heriot-Watt University authors would like to acknowledge and thank the Airguide Photonics team for their support in this project.

Disclosures. The authors declare no conflicts of interest.

Data availability. Data underlying the results presented in this paper are available in Ref. [33].

REFERENCES

1. N. Gisin, G. Ribordy, W. Tittel, and H. Zbinden, "Quantum cryptography," Rev. Mod. Phys. **74**, 145 (2021).
2. V. Scarani, H. Bechmann-Pasquinucci, N. J. Cerf, M. Dušek, N. Lütkenhaus, and M. Peev, "The security of practical quantum key distribution," Rev. Mod. Phys. **81**, 1301–1350 (2009).
3. M. Avesani, L. Calderaro, M. Schiavon, A. Stanco, C. Agnesi, A. Santamato, M. Zahidy, A. Scriminich, G. Foletto, G. Contestabile, M. Chiesa, D. Rotta, M. Artiglia, A. Montanaro, M. Romagnoli, V. Sorianello, F. Vedovato, G. Vallone, and P. Villoresi, "Full daylight quantum-key-distribution at 1550 nm enabled by integrated silicon photonics," npj Quantum Inf. **7**, 93 (2021).
4. S. Pirandola, U. L. Andersen, L. Banchi, M. Berta, D. Bunandar, R. Colbeck, D. Englund, T. Gehring, C. Lupo, C. Ottaviani, J. L. Pereira, M. Razavi, J. Shamsul Shaari, M. Tomamichel, V. C. Usenko, G. Vallone, P. Villoresi, and P. Wallden, "Advances in quantum cryptography," Adv. Opt. Photon. **12**, 1012–1236 (2020).
5. E. Diamanti, H. K. Lo, B. Qi, and Z. Yuan, "Practical challenges in quantum key distribution," npj Quantum Inf. **2**, 16025 (2016).
6. B. Lovitz and N. Lütkenhaus, "Families of quantum fingerprinting protocols," Phys. Rev. A **97**, 032340 (2018).
7. R. J. Donaldson, R. J. Collins, K. Kleczkowska, R. Amiri, P. Wallden, V. Dunjko, J. Jeffers, E. Andersson, and G. S. Buller, "Experimental demonstration of kilometer-range quantum digital signatures," Phys. Rev. A **93**, 012329 (2016).
8. R. Amiri, R. Stárek, D. Reichmuth, I. V. Puthoor, M. Mičuda, Jr., L. Mišta, M. Dušek, P. Wallden, and E. Andersson, "Imperfect 1-out-of-2 quantum oblivious transfer: bounds, a protocol, and its experimental implementation," PRX Quantum. **2**, 010335 (2021).
9. M. Lucamarini, Z. L. Yuan, J. F. Dynes, and A. J. Shields, "Overcoming the rate-distance limit of quantum key distribution without quantum repeaters," Nature **557**, 400–403 (2018).
10. Y. Liu, Z. W. Yu, W. Zhang, J. Y. Guan, J. P. Chen, C. Zhang, X. L. Hu, H. Li, C. Jiang, J. Lin, T. Y. Chen, L. You, Z. Wang, X. B. Wang, Q. Zhang, and J. W. Pan, "Experimental twin-field quantum key distribution through sending or not sending," Phys. Rev. Lett. **123**, 100505 (2019).
11. M. Minder, M. Pittaluga, G. L. Roberts, M. Lucamarini, J. F. Dynes, Z. L. Yuan, and A. J. Shields, "Experimental quantum key distribution beyond the repeaterless secret key capacity," Nat. Photonics **13**, 334–338 (2019).
12. Y. Shi, S. Moe Thar, H. S. Poh, J. A. Grieve, C. Kurtsiefer, and A. Ling, "Stable polarization entanglement based quantum key distribution over a deployed metropolitan fiber," Appl. Phys. Lett. **117**, 124002 (2020).
13. A. Boaron, B. Korzh, R. Houlmann, G. Boso, D. Rusca, S. Gray, M. J. Li, D. Nolan, A. Martin, and H. Zbinden, "Simple 2.5 GHz time-bin quantum key distribution," Appl. Phys. Lett. **112**, 171108 (2018).
14. S. K. Liao, W. Q. Cai, W. Y. Liu, *et al.*, "Satellite-to-ground quantum key distribution," Nature **549**, 43–47 (2017).
15. S. Ecker, B. Liu, J. Handsteiner, M. Fink, D. Rauch, F. Steinlechner, T. Scheidl, A. Zeilinger, and R. Ursin, "Strategies for achieving high key rates in satellite-based QKD," npj Quantum Inf. **7**, 1–7 (2021).
16. A. Boaron, G. Boso, D. Rusca, C. Vulliez, C. Autebert, M. Caloz, M. Perrenoud, G. Gras, F. Bussières, M. J. Li, D. Nolan, A. Martin, and H. Zbinden, "Secure quantum key distribution over 421 km of optical fiber," Phys. Rev. Lett. **121**, 190502 (2018).
17. F. B. Basset, M. Valeri, E. Roccia, V. Muredda, D. Poderini, J. Neuwirth, N. Spagnolo, M. B. Rota, G. Carvacho, F. Sciarrino, and R. Trotta, "Quantum key distribution with entangled photons generated on demand by a quantum dot," Sci. Adv. **7**, eabe6379 (2021).
18. H. H. Diamandi and A. Zadok, "Opto-mechanical inter-core cross-talk in multi-core fibers," in *Optics InfoBase Conference Papers* (The Optical Society, 2021).
19. I. Choi, R. J. Young, and P. D. Townsend, "Quantum information to the home," New J. Phys. **13**, 063039 (2011).
20. J. F. Dynes, S. J. Kindness, S. W.-B. Tam, A. Plews, A. W. Sharpe, M. Lucamarini, B. Fröhlich, Z. L. Yuan, R. V. Penty, and A. J. Shields, "Quantum key distribution over multicore fiber," Opt. Express **24**, 8081–8087 (2016).
21. B.-X. Wang, Y. Mao, L. Shen, L. Zhang, X.-B. Lan, D. Ge, Y. Gao, J. Li, Y.-L. Tang, S.-B. Tang, J. Zhang, T.-Y. Chen, and J.-W. Pan, "Long-distance transmission of quantum key distribution coexisting with classical optical communication over a weakly-coupled few-mode fiber," Opt. Express **28**, 12558–12565 (2020).
22. G. B. Xavier and G. Lima, "Quantum information processing with space-division multiplexing optical fibres," Commun. Phys. **3**, 9 (2020).
23. D. J. Richardson, J. M. Fini, and L. E. Nelson, "Space-division multiplexing in optical fibres," Nat. Photonics **7**, 354–362 (2013).
24. D. Bacco, B. da Lio, D. Cozzolino, F. da Ros, X. Guo, Y. Ding, Y. Sasaki, K. Aikawa, S. Miki, H. Terai, T. Yamashita, J. S. Neergaard-Nielsen, M. Galili, K. Rottwitt, U. L. Andersen, T. Morioka, and L. K. Oxenløwe, "Boosting the secret key rate in a shared quantum and classical fibre communication system," Commun. Phys. **2**, 140 (2019).
25. W. Ni, C. Yang, Y. Luo, R. Xia, P. Lu, D. J. J. Hu, S. Danto, P. P. Shum, and L. Wei, "Recent advancement of anti-resonant hollow-core fibers for sensing applications," Photonics **8**, 128 (2021).
26. F. Poletti, "Nested antiresonant nodeless hollow core fiber," Opt. Express **22**, 23807–23828 (2014).
27. H. Sakr, Y. Chen, G. T. Jasion, T. D. Bradley, J. R. Hayes, H. C. H. Mulvad, I. A. Davidson, E. Numkam Fokoua, and F. Poletti, "Hollow core optical fibres with comparable attenuation to silica fibres between 600 and 1100 nm," Nat. Commun. **11**, 6030 (2020).
28. O. Alia, R. S. Tessinari, T. D. Bradley, H. Sakr, K. Harrington, J. Hayes, Y. Chen, P. Petropoulos, D. Richardson, F. Poletti, G. T. Kanellos, R. Nejabati, and D. Simeonidou, "1.6 Tbps classical channel coexistence with DV-QKD over hollow core nested antiresonant

nodeless fibre (HC-NANF)," in *European Conference on Optical Communication (ECOC)* (IEEE, 2021), pp. 1–4.
29. X. Chen, W. Ding, Y.-Y. Wang, S.-F. Gao, F. Xu, H. Xu, Y.-F. Hong, Y.-Z. Sun, P. Wang, Y.-Q. Lu, and L. Zhang, "High-fidelity, low-latency polarization quantum state transmissions over a hollow-core conjoined-tube fiber at around 800 nm," Photon. Res. **9**, 460–470 (2021).
30. G. T. Jasion, T. D. Bradley, K. Harrington, H. Sakr, Y. Chen, E. N. Fokoua, I. A. Davidson, A. Taranta, J. R. Hayes, D. J. Richardson, and F. Poletti, "Hollow core NANF with 0.28 dB/km attenuation in the C and L bands," in *Optical Fiber Communication Conference Postdeadline Papers* (OSA, 2020), paper Th4B.4.
31. D. Stucki, C. Barreiro, S. Fasel, J.-D. Gautier, O. Gay, N. Gisin, R. Thew, Y. Thoma, P. Trinkler, F. Vannel, and H. Zbinden, *Continuous High Speed Coherent One-Way Quantum Key Distribution* (APD, 2009).
32. J. Gonzalez-Payo, R. Trenyi, W. Wang, and M. Curty, "Upper security bounds for coherent-one-way quantum key distribution," Phys. Rev. Lett. **125**, 260510 (2020).
33. U. Nasti, H. Sakr, I. A. Davidson, F. Poletti, and R. J. Donaldson, "Utilising broadband wavelength-division multiplexing capabilities of hollow-core fiber for quantum communications dataset," Heriot Watt University, (2022), https://doi.org/10.17861/d42d3df1-661d-41bf-8bf6-c04d61d021a7.